

1 **The Indonesian Throughflow Circulation Under Solar**
2 **Geoengineering**

3 Chencheng Shen¹ John C. Moore^{1,2*} Heri Kuswanto^{3,4} Liyun Zhao^{1*}

4 ¹State Key Laboratory of Earth Surface Processes and Resource Ecology, Faculty of Geographical
5 Science, Beijing Normal University, Beijing 100875, China

6 ²Arctic Centre, University of Lapland, Rovaniemi, Finland

7 ³Center for Disaster Mitigation and Climate Change, Institut Teknologi Sepuluh Nopember, Surabaya,
8 Indonesia.

9 ⁴Department of Statistics, Institut Teknologi Sepuluh Nopember, Surabaya, Indonesia.

10 *Correspondence to:* john.moore.bnu@gmail.com, zhaoliyun@bnu.edu.cn

11

12 Short summary (less than 500 characters):

13 The Indonesia Throughflow is an important pathway connecting the Pacific and Indian Oceans and is
14 part of a wind-driven circulation that is expected to reduce under greenhouse gas forcing. Solar dimming
15 and sulfate aerosol injection geoengineering may reverse this effect. But stratospheric sulfate aerosols
16 affects winds more than simply “shading the sun” and hence reduces the water transport similar as we
17 simulate for unabated greenhouse gas emissions.

18

19

20 **Abstract**

21 The Indonesia Throughflow (ITF) is the only low-latitude channel between the Pacific and Indian oceans,
22 and its variability has important effects on global climate and biogeochemical cycles. Climate models
23 consistently predict a decline in ITF transport under global warming, but it has not yet been examined
24 under solar geoengineering scenarios. We use standard parameterized methods for estimating ITF: the
25 Amended Island Rule and Buoyancy Forcing, to investigate ITF under the SSP2-4.5 and SSP5-8.5
26 greenhouse gas scenarios, and the geoengineering experiments G6solar and G6sulfur that reduce net
27 global mean radiative forcing from SSP5-8.5 levels to SSP2-4.5 levels using solar dimming and sulfate
28 aerosol injection strategies. Six model ensemble mean projections for 2080 - 2100 relative to historical

29 (1980-2014) ITF are reductions of 19% under the G6solar scenario and 28% under the G6sulfur scenario
30 which compare with reductions of 23% and 27% under SSP2-4.5 and SSP5-8.5. Despite standard
31 deviations amounting to 5-8% for each scenario, all scenarios are significantly different from each other
32 ($p < 0.05$) when taken over the whole 2020-2100 simulation period. Thus, significant weakening of the
33 ITF occurs under all scenarios, but G6solar closer approximates SSP2-4.5 than does G6sulfur. In contrast
34 with the other three scenarios which show only reductions in forcing due to ocean upwelling, the G6sulfur
35 experiment shows a large reduction in ocean surface wind stress forcing accounting for 47% (38% - 65%
36 across model range) of the decline of Wind+Upwelling ITF transport. There are also reductions in deep-
37 sea upwelling in extratropical western boundary currents.

38

39 **1. Introduction**

40 The Indonesian Throughflow (ITF) is an important part of the global thermohaline circulation (Gordon,
41 1986; Lee et al., 2002; Sprintall et al., 2009). The ITF brings about 15 Sv (1 Sv = 10^6 m³/s; ~10.7 to ~18.7
42 Sv during the INSTANT Field Program, 2004-2006) of warm and fresh water from the Pacific to the
43 Indian Ocean (Sprintall et al., 2009). Since the ITF is the only ocean pathway in the tropics between the
44 Pacific and Indian Oceans it is the key to heat and water volume transport between them (Godfrey, 1996;
45 Talley, 2008). The ITF also plays an important role in regulating global climate and biogeochemical
46 cycles (Ayers et al., 2014; Hirst and Godfrey, 1994), for example the ITF may influence the El Nino-
47 Southern Oscillation (ENSO) by altering the tropical-subtropical exchange, the structure of the mean
48 tropical thermocline, and the mean sea surface temperature (SST) difference between the Pacific warm
49 Pool and the cold tongue, etc. (Lee et al., 2002) and in the supply of iron in the equatorial upwelling,
50 maintaining biological production in the equatorial eastern Pacific (Gorgues et al., 2007). Sen Gupta et
51 al. (2021) used 26 CMIP6 models to predict ITF weakening by 3 Sv (2.4-3.2 Sv model range) under the
52 SSP5-8.5 scenario (the high greenhouse gas emission scenario) relative to 20th century historical means
53 The decline in the ITF would lead to more heat to accumulate in the Pacific Ocean, which could alter
54 tropical atmospheric-ocean interactions and contribute to extreme El Nino /La Nina events (Cai et al.,
55 2015; Klinger and Garuba, 2016).

56

57 The ITF is fed by the Mindanao Current and the New Guinea Coast Undercurrent (Figure 1) and, to a
58 lesser extent, parts of the low-latitude Pacific Western Boundary Current (WBC) that flows toward the
59 equator (Godfrey, 1996; Lukas et al., 1996). The ITF helps supply the Agulhas current leakage from the
60 Indian Ocean to the South Atlantic Ocean, and may be said to flush Indian Ocean thermocline waters
61 southward by boosting the Agulhas current (Durgadoo et al., 2017; Gordon, 2005).

62

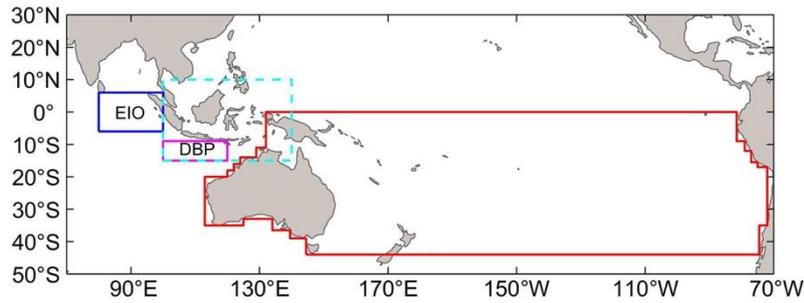
63 The interannual and decadal variability of the ITF transport is influenced by surface winds in the Pacific
64 and Indian Oceans (Feng et al., 2011; Meyers, 1996). Wyrcki (1987) noticed that the pressure gradient
65 between the Pacific and Indian Oceans dominates the ITF flux, and hence that sea level is a good indicator
66 of upper-ocean ITF transport. The largest volume flux is in July-August and the lowest in January-
67 February.

68

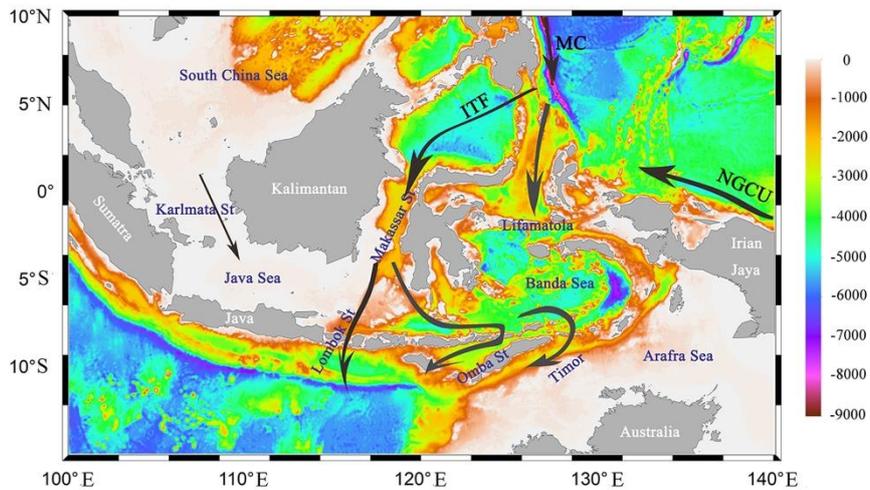
69 Model simulations consistently project that ITF transport will be weakened by increased greenhouse gas
70 (GHG) forcing (Feng et al., 2012; Hu et al., 2015; Sen Gupta et al., 2021; Vecchi and Soden, 2007). The
71 driving force is the weakening of the Pacific trade winds under global warming in the 21st century which
72 then weaken the Mindanao Current, the main inflow route of the ITF (Alory et al., 2007; Duan et al.,
73 2017; Sen Gupta et al., 2012).

74

a) The wind stress integral path and buoyancy region



b) Topography of Indonesian Sea



75

76 Figure 1. (a) The red line is the wind stress integral path for the Island Rule, The Downstream Buoyant
77 Pool (magenta box) and Equatorial Indian Ocean (blue box) where the density difference is the main
78 index to calculate the ITF transport by buoyancy forcing. (b) Inset defined by the cyan dotted line in the
79 panel (a) showing the offshore bathymetry in the maritime continent (ETOPO Global Relief Model,
80 (Amante and Eakins, 2009)) and the Mindanao Current (MC), and the New Guinea Coast Undercurrent
81 (NGCU) paths contributing to the ITF.

82

83 Analyzing the water flux through the many shallow channels in the Indonesian archipelago is challenging,
84 and many of these channels are not resolved in simulations with resolutions of a degree or so (Gordon et
85 al., 1999) (Figure 1). This motivates use of alternative methods of estimating ITF. Godfrey (1989) created
86 the Island Rule to estimate flux based on Sverdrup theory (Sverdrup, 1947) analysis of Pacific wind
87 stress. More recently, analysis of climate models revealed the importance of deep ocean circulation to
88 the reduction of ITF transport under GHG forcing. The decline in ITF under GHG forcing could be due

89 to both the weakening of trade winds in the Pacific, and deep ocean circulation changes (Feng et al.,
90 2012; Hu et al., 2015). Interannual to decadal, as well as centennial dependence of the ITF on wind and
91 upwelling was found with an eddy-resolving ocean model simulation (Feng et al., 2017). This led to Sen
92 Gupta et al. (2016), and Feng et al. (2017) proposing the Amended Island Rule that modifies the Island
93 Rule to include the estimated net Pacific upwelling contribution to ITF based on high-resolution ($1/10^\circ$)
94 ocean general circulation modelling.

95

96 An alternative mechanism for the ITF driver was proposed earlier by Andersson and Stigebrandt (2005).
97 In this theory buoyancy forcing is more important than wind forcing in driving the ITF. The ITF
98 variability is found from the baroclinic outflow of the Downstream Buoyant Pool (DBP) that extends
99 over much of the North Australian Basin (Figure 1). Hu and Sprintall (2016) used this method with
100 reanalysis products to produce ITF interannual variability in good agreement with the observed volume
101 transports (2004–2006) from the INSTANT mooring array transport (Sprintall et al., 2009), although the
102 average transport was only half the transport observed during INSTANT. INSTANT uses moorings
103 deployed at the major inflow (Makassar Strait, Lifamatola Strait) and outflow passages (Lombok Strait,
104 Ombai Strait and Timor Passage) of the ITF to estimate the ITF transport, resulting in a value of 15 Sv
105 during 2004-2006. In contrast with the reasonable agreement for the Amended Island Rule estimates of
106 ITF, the alternative buoyancy method behaves much worse, indicating that the hypothetical forcing is
107 not as good an explanation for ITF as the Amended Island Rule, or that the models used do not capture
108 the specific details of the DBP. But although the Amended Island Rule matches the short duration of
109 observed fluxes and variability better than buoyancy, it is possible that changes in buoyancy forcing may
110 affect volume transport of the ITF on decadal scales under a changing climate and so we examine its
111 changes under the geoengineering scenarios.

112

113 Solar Radiation Modification (SRM) geoengineering is designed to reduce the solar radiation reaching
114 the surface of the earth and slow down climate warming due to GHG forcing (Shepherd, 2009). Since
115 SRM shortwave forcing has different spatial and temporal variability than longwave forcing, it can only
116 imperfectly offset the climate change caused by the increase of GHGs. In this article we focus on two

117 styles of SRM: reduction of the solar constant to mimic the effect of a sunshade, called solar dimming
118 (SD); and stratospheric aerosol injection (SAI), specifically with injection of sulfate aerosol in the
119 tropical lower stratosphere (Kravitz et al., 2015). These styles of SRM are known to produce over-cooled
120 tropical oceans and under-cooled poles relative to global mean temperatures. However, other styles of
121 injection strategies than the simple tropical site specified by G6 can produce simulated climates without
122 these temperature biases (MacMartin and Kravitz, 2016). Simulated tropical atmospheric circulation
123 systems are impacted under both GHG and solar geoengineering scenarios. Under SD, the seasonal
124 movement of the intertropical convergence zone is reduced relative to GHG climates (Smyth et al., 2017).
125 Both the Hadley and Walker circulations are different from the historical (Cheng et al., 2022; Guo et al.,
126 2018). Impacts of SRM on the Walker circulation are modest compared with the Hadley cell but appear
127 most obviously in relation to the South Pacific Convergence Zone (Guo et al., 2018), which is relevant
128 in the overall tropical Pacific atmosphere system that drives and interacts with the ITF. Greenhouse gas
129 forcing is expected to cause an expansion of the Hadley circulation cells which may be asymmetric
130 between northern and southern hemispheres (Staten et al., 2019). Both SD (Guo et al., 2018) and SAI
131 (Cheng et al., 2022) reduce these greenhouse gas induced changes in the Hadley circulation, although
132 again hemispheric differences remain, and in the Cheng et al. (2022) simulations, were associated with
133 stratospheric heating and tropospheric temperature response due to enhanced stratospheric aerosol
134 concentrations. The changes in stratospheric heating, the tropopause height, and tropical sea surface
135 temperatures may be expected to impact tropical cyclogenesis, and this is consistent with reduction in
136 North Atlantic hurricane numbers and intensity relative to GHG-only climates under SAI (Moore et al.,
137 2015). However, there are differences between tropical basins in expected tropical cyclogenesis potential
138 and significant differences in simulations between climate models (Wang et al., 2018). Potential energy
139 available for extratropical storms is also consistently reduced under SRM relative to GHG
140 forcing (Gertler et al., 2020). The reported impacts highlight the potential role of wind forcing in ITF.

141

142 Little research to date has been done on ocean circulation under SRM, with only the Atlantic Meridional
143 Overturning Circulation (AMOC) having been studied in depth (Hong et al., 2017; Moore et al., 2019;
144 Muri et al., 2018; Tilmes et al., 2020; Xie et al., 2022). Both GHG forcing alone, and with SRM, produce

145 a weakening of AMOC relative to present day, mainly in response to the change of heat flux in the North
146 Atlantic, with little influence from the changes of freshwater flux and wind stress (Hong et al., 2017; Xie
147 et al., 2022). AMOC is less weakened under SRM than with GHG forcing alone and the AMOC declines
148 seen under GHG forcing are consistently reversed by SRM towards present day patterns (Moore et al.,
149 2019; Muri et al., 2018; Tilmes et al., 2020).

150

151 In this study, we will examine the impact of SRM on the change of the ITF in the 21st century, and
152 consider the transport and drivers differences between pure GHG climates representing moderate
153 mitigation (SSP2-4.5) and no mitigation (SSP5-8.5); with solar dimming (G6solar) and stratospheric
154 aerosol injection (G6sulfur) forms of SRM geoengineering.

155

156 **2. Climate Models and Scenarios**

157 The Intergovernmental Panel on Climate Change (IPCC) Shared Socioeconomic Pathways (SSPs) are
158 scenarios defined by radiative forcing goals to be achieved through various climate mitigation policy
159 alternatives (Kriegler et al., 2012; van Vuuren et al., 2011). The climate model simulation results under
160 the SSPs are being performed as part of the Coupled Model Intercomparison Project Phase 6 (CMIP6).
161 We used CMIP6 historical simulation during 1980-2014 (Eyring et al., 2016) and two GHG scenarios
162 during 2015-2100: SSP5-8.5, an unmitigated GHG emission scenario which raises mean global radiative
163 forcing by 8.5 W/m^2 over pre-industrial levels at 2100; and SSP2-4.5 designed to reach peak radiative
164 forcing of 4.5 W/m^2 by mid-century (O'Neill et al., 2016). We use the Geoengineering Model
165 Intercomparison Project Phase 6 (GeoMIP6) G6sulfur and G6solar scenarios during 2020-2100 (Kravitz
166 et al., 2015). The G6sulfur experiment specifies using SAI to reduce the net anthropogenic radiative
167 forcing constantly during the 2020-2100 period from the SSP5-8.5 to the SSP2-4.5 level, while G6solar
168 does the same using SD (Kravitz et al., 2015). The two SRM methods produce significantly different
169 surface climates, with differences from SSP2-4.5 being larger and more spatially variable under G6sulfur
170 than G6solar (Visioni et al., 2021). While the G6 scenarios are not particular realistic, for example they
171 specify starting SAI in 2020 and specify a very simple tropical injection strategy, they do provide a
172 usefully large SRM and GHG signal, and have been simulated by six CMIP6 generation models. This

173 allows more robust findings of the general impacts of SAI, especially when considering aspects of the
174 climate system that have not been addressed to date in geoengineering studies, such as the ITF.

175

176 We used monthly data from the first realization in each scenario from all six Earth System Models (ESM;
177 Table 1) that have performed the CMIP6 and GeoMIP6 scenarios to estimate the ITF transport. The
178 variable fields we use are zonal and meridional wind stress (τ_{uu} and τ_{vv}), sea water vertical velocity
179 (w_o), sea water salinity and temperature (s_o and $\theta_{o,s}$). All fields were bi-linearly interpolated (except
180 for sea water vertical velocity, for which we use conservative interpolation) onto a common $0.5^\circ \times 0.5^\circ$
181 grid.

182

183 **Table 1**

184 *Earth System Models (ESMs) Used in This Study*

Model	Atmospheric Resolution (long \times lat)	Ocean Resolution (long \times lat)	Reference
CESM2-WACCM	288 \times 192	320 \times 384	(Danabasoglu et al., 2020)
CNRM-ESM2-1	256 \times 128	362 \times 294	(Séférian et al., 2019)
IPSL-CM6A-LR	144 \times 143	320 \times 384	(Boucher et al., 2020)
MPI-ESM1-2-HR	384 \times 192	802 \times 404	(Mauritsen et al., 2019)
MPI-ESM1-2-LR	192 \times 96	256 \times 220	(Mauritsen et al., 2019)
UKESM1-0-LL	192 \times 144	360 \times 330	(Sellar et al., 2019)

185

186 **3. Methods**

187 **3.1 Island Rule**

188 In the Sverdrup balance, ocean current acceleration and friction are neglected, and wind stress curl is the
189 driving force of large-scale ocean circulation (Sverdrup, 1947). The “Island Rule” (Godfrey, 1989) uses
190 the Sverdrup balance to calculate the net total flow through a region by the integral of the wind stress on
191 a specific closed path. This is a simple and more efficient way of estimating the long-term magnitude
192 and interannual variability than direct observations of flow through the complex channel topography and
193 equator spanning Indonesian archipelago (Godfrey, 1996). Feng et al. (2011) used an eddy-permitting

194 numerical model, ORCA025, to verify that the Island Rule can capture the decadal variability of the ITF
195 transport.

196

197 The original Island Rule assumes that the ocean is dormant below a moderate depth, Z , below which
198 there is no motion (Sverdrup, 1947). The ITF transport is determined by the integral of wind stress along
199 the path from the southern tip of Australia, eastwards to South America, following the coastline to the
200 latitude line of the northwestern tip of Papua New Guinea (PNG) and then traces the west coast of
201 Australia back to the starting point (Figure 1a):

$$202 \quad T_{ITF} = \frac{1}{f_N - f_S} \oint \frac{\tau^l}{\rho_0} dl \quad (1)$$

203 where f_N and f_S are the Coriolis parameter at the equator and 44°S, respectively. τ^l is the along route
204 wind stress component. ρ_0 is the mean sea water density.

205

206 **3.2 Amended Island Rule**

207 Studies have suggested that a decline in ITF under GHG forcing was due to both the weakening of trade
208 winds in the Pacific, and the impact of the deep ocean circulation change (Feng et al., 2012; Hu et al.,
209 2015). Sen Gupta et al. (2016) used a climate model to attribute GHG-forced decrease of the ITF transport
210 to weakening of deep Pacific upwelling. Feng et al. (2017) estimated the contribution of deep ocean
211 upwelling from the Pacific north of 44°S to produce the Amended Island Rule:

$$212 \quad T_{ITF} = \frac{1}{f_N - f_S} \oint \frac{\tau^l}{\rho_0} dl + \iint_{pacific} w_z ds \quad (2)$$

213 where w_z is the vertical velocity of the Pacific at 1500 m depth. The contribution of deep ocean upwelling
214 is integrated over the whole Pacific north of 44°S (considering volume conservation and the sill depths
215 of the Indonesian seas is less than 1500m). The Amended Island Rule was verified with a near-global
216 eddy-resolving ocean model simulation, and found to well-estimate the interannual to decadal, as well
217 as centennial variabilities of the ITF transport (Feng et al., 2017). Here we describe the ITF using the
218 Amended Island Rule, and its component parts which are the wind driven Sverdrup balance, and the
219 Pacific upwelling.

220

221 3.3 Buoyancy Forcing

222 Sea levels in the Pacific and Indian Oceans have been used to estimate the ITF transport in previous
223 studies (Clarke and Liu, 1994; Potemra et al., 1997; Susanto and Song, 2015). Buoyancy accounts for
224 high steric sea level (that is a volume increase due to lower density) in the North Pacific (Stigebrandt,
225 1984). A pool of low-density water (the DBP) originating in the North Pacific is formed in the eastern
226 Indian Ocean between the Indonesian islands and northwestern Australia (Figure 1a). The sea level drop
227 between Indian and Pacific Oceans occurs essentially at the abrupt eastern boundary of the DBP and is
228 the source of buoyancy forcing (Andersson and Stigebrandt, 2005). In the DBP region, the long-term
229 difference between the westward and eastward transport along the northern and southern flanks of the
230 pool is the ITF transport.

231

232 The geostrophic transport in the DBP is related to denser water in the eastern equatorial Indian Ocean
233 (EIO):

$$234 \quad Q_{\lambda} = \frac{gH^2\Delta\rho}{2f_{\lambda}\rho_0} \quad (3)$$

$$235 \quad ITF = Q_{\lambda_N} - Q_{\lambda_S} \quad (4)$$

236 where g is acceleration due to gravity, H is the penetration depth of the DBP (set by (Andersson and
237 Stigebrandt, 2005) as 1200 m), f_{λ} is the Coriolis parameter at latitude λ , ρ_0 is the reference density at
238 1200 m, The northern (λ_N) and southern (λ_S) boundary latitudes of the DBP are 10°S and 16°S
239 respectively. $\Delta\rho$ is the density difference between the DBP region (9°S – 15°S , 100°E – 120°E) and the EIO
240 region (6°N – 6°S , 80°E – 100°E). Hu and Sprintall (2016) verified the use of DPB and EIO to calculate
241 $\Delta\rho$ with observations.

242

243 4. Transport and Geoengineering

244 4.1 ITF Transport

245 The multi-model ensemble mean wind driven ITF transport is ~ 16.9 Sv with the Pacific upwelling north
246 of 44°S contributing ~ 4.5 Sv in the historical period (Figure 2). This compares with observational
247 estimates of about 15 Sv during 2004-2006 (Sprintall et al., 2009) and the multi-model ensemble (total
248 22 CMIP5 models) mean is 15.2 Sv during 1900-2000 (Sen Gupta et al., 2016). Under SSP2-4.5 during

249 2015 - 2100, the wind-driven and Pacific upwelling contributions to ITF transport are not much different
250 from those under SSP5-8.5. The wind driven volume ITF transport has significant trends for all scenarios
251 with smallest trends for the SSP scenarios (linear trends of lower magnitude than 0.02 Sv per year), while
252 the upwelling contributions has obvious downward trends in all scenarios. These trends appear to be
253 consistent, despite differences in estimated transport across models (Figure S1). Thus the decline in future
254 ITF transport in future GHG climates was explained by (Feng et al., 2017) as due to weakening of the
255 Pacific upwelling on centennial timescales while wind-driven processes had no impact on long
256 timescales.

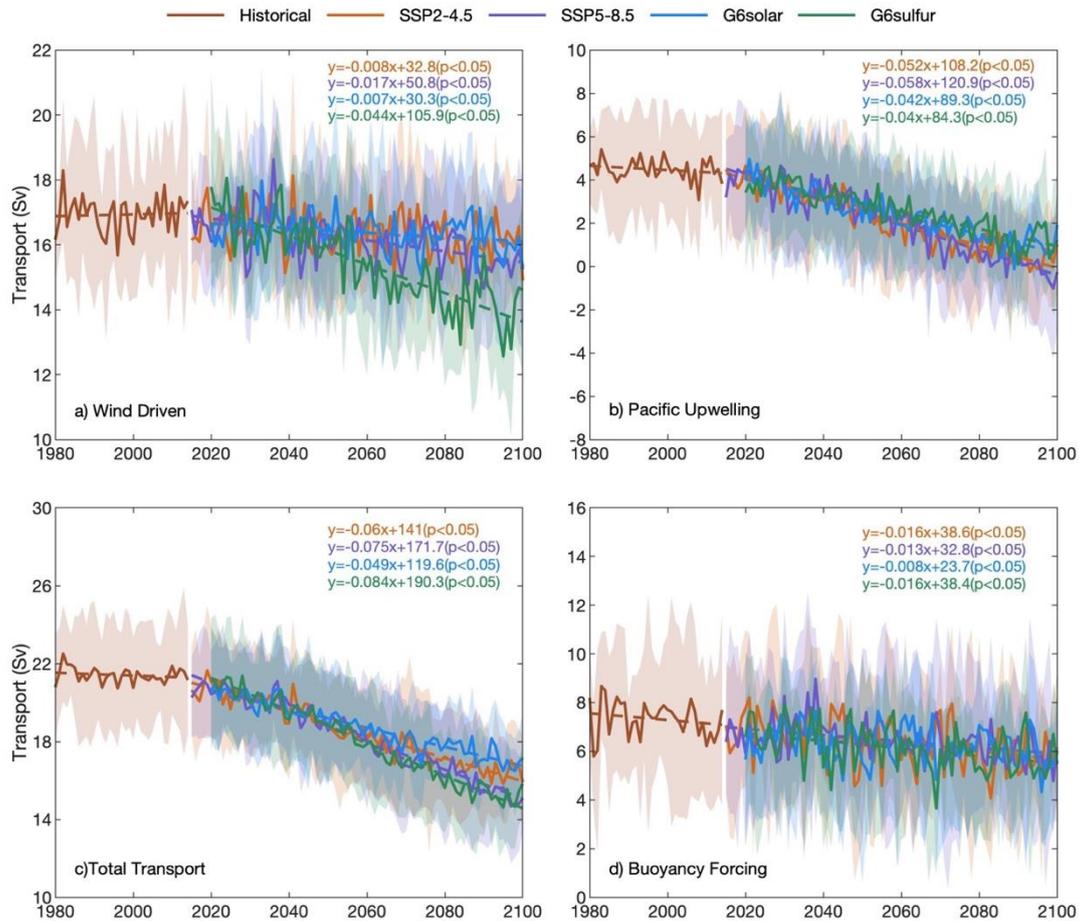
257

258 During the last 20 years of the 21st century, the simulated ITF transport using the Amended Island Rule
259 is $27\% \pm 3\%$ (standard error) under SSP5-8.5 (Figure 2c), with Pacific upwelling decline accounting for
260 $76\% \pm 15\%$ ($p < 0.05$, Wilcoxon signed rank test) of the Wind+Upwelling reduction. Both wind driven and
261 upwelling contributions to ITF transport are slightly higher under SSP2-4.5 than under SSP5-8.5 during
262 the same period, but the differences are small over the whole 2015-2100 period. The Wind+Upwelling
263 ITF transport is reduced by $23\% \pm 2\%$ (standard error, $p < 0.05$) under SSP2-4.5 during the period of 2080-
264 2100 relative to the historical period (13%~27% cross ESM range), and with the wind driven component
265 only dropping by 5% (-2%~9% range). The reductions under SSP5-8.5 for upwelling and wind driven
266 components are respectively 97% (60%~305%) and 8% (1%~19%).

267

268 In contrast with the reasonable agreement for the Amended Island Rule estimates of ITF, the alternative
269 buoyancy method behaves much worse. The multi-mean ITF transport simulated by buoyancy forcing is
270 7.3 Sv in the historical period, which is less than that by wind driven and only half the transport observed
271 during INSTANT (Sprintall et al., 2009), and there is large across-model variability (Figure S2). Under
272 the two SSPs scenarios, the difference in ITF transport is small with significant trend during 2015-2100.
273 The buoyancy driven estimation method can capture the interannual variability of ITF transport, but it
274 does not perform well on centennial timescales (Hu and Sprintall, 2016), where ITF is much closer to
275 that from the wind driven estimation method.

276



277

278 **Figure 2.** Six ESM ensemble mean ITF components under different scenarios, shadings show the
 279 standard deviation and the equation are the regression trend lines (2015-2100 under the two SSP
 280 scenarios and 2020-2100 under the two G6 scenarios) and the significance of the slope, (a) Sverdrup
 281 balance wind driven component. (b) Pacific upwelling north of 44°S. (c) Wind+Upwelling ITF under
 282 the Amended Island Rule (Eq 2). (d) ITF transport by buoyancy forcing. Individual ESM results are
 283 shown in Figure S1.

284

285 SAI and SD geoengineering methods clearly have different impacts on wind driven contributions to ITF
 286 transport for all models (Table S1) and the ensemble mean (Table 2) according to the Wilcoxon signed-
 287 rank test, and smaller although still significant differences in upwelling for the 6 model ensemble mean,
 288 although significant differences individually only for CESM2-WACCM (Figure 2a,b, Table 2; Table S1).
 289 Under the G6solar and G6sulfur scenarios, the Wind+Upwelling ITF transport is reduced by 19%±1%
 290 and 28%±1% respectively during 2080 - 2100 relative to the historical period, of which the wind-driven

291 ITF transport is reduced by $4\% \pm 1\%$ and $16\% \pm 1\%$, and the upwelling transport volume is reduced by
 292 $76\% \pm 8\%$ and $70\% \pm 10\%$, all these differences between scenarios are significant ($p < 0.05$, Wilcoxon
 293 signed-rank test; Table 2). Under G6sulfur, the wind driven ITF transport has a clear downward trend in
 294 contrast with the other three climate scenarios (Figure 2a). Each ESM also shows consistency in the
 295 relative declines under the four future climates (Figure S1a). The decline of wind driven transport
 296 accounts for 47% (38% - 65% range) of the decline of Wind+Upwelling ITF transport under G6sulfur
 297 during 2080-2100, and its ensemble mean wind driven transport volume is significantly lower than that
 298 under SSP5-8.5 (Table 2). The ensemble mean ITF transport by buoyancy forcing all have significant
 299 declining trend under the future climate scenarios but the differences are not generally significant (Figure
 300 2d, Table 2), which is different from the transport change calculated using the wind driven and upwelling
 301 contributions.

302

303 **Table 2**

304 The differences in monthly ITF Transport (2020-2100)^a and its components according to the different
 305 methods; Wind is the ITF transport derived from Island Rule and used in the Amended Island Rule;
 306 Upwelling is the area integral of Pacific upwelling rate at 1500 m used in the Amended Island Rule;
 307 Wind+Upwelling is the ITF transport calculated by Amended Island Rule; Buoyancy is the ITF transport
 308 by buoyancy forcing and used independently of the other two components. Unit: Sv ($1\text{Sv} = 10^6 \text{ m}^3/\text{s}$)

309

Differences	Wind	Upwelling	Wind+Upwelling	Buoyancy
G6solar – SSP2-4.5	0.02	0.33	0.35	-0.06
G6sulfur – SSP2-4.5	-0.96	0.53	-0.44	-0.21
G6solar – SSP5-8.5	0.23	0.4	0.63	-0.15
G6sulfur – SSP5-8.5	-0.75	0.59	-0.16	-0.3
G6sulfur –G6solar	-0.98	0.19	-0.79	-0.15

310

311 ^aThe end dates of the G6solar and G6sulfur of MPI-ESM1-2-HR are 2099 and 2089, respectively, and
 312 those of MPI-ESM1-2-LR are both in 2099. Values in bold are significant at the 95% level according
 313 to the Wilcoxon signed-rank test.

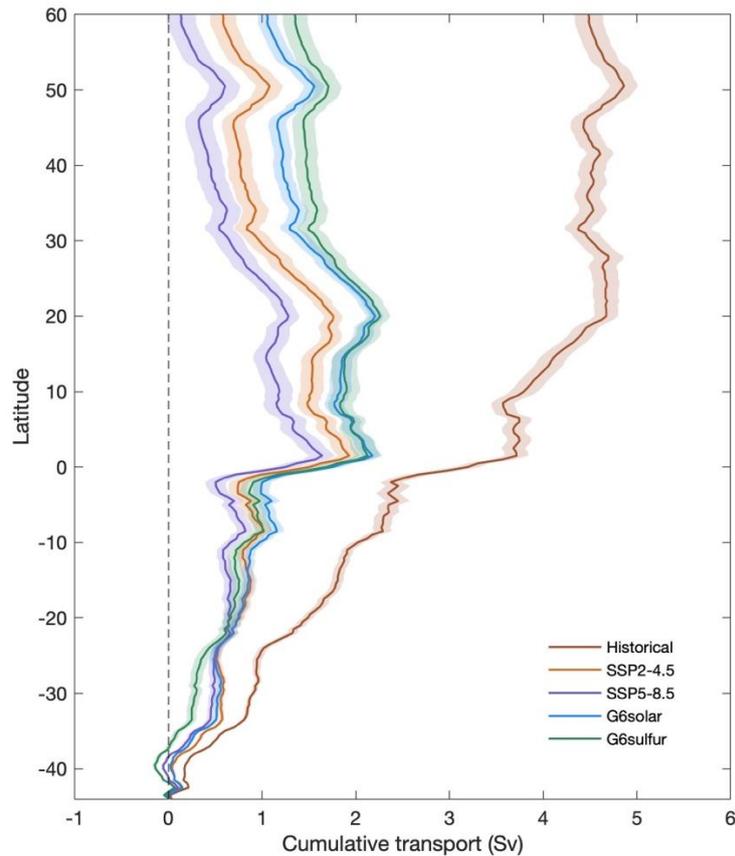
314

315

316 The decline in ITF transport via upwelling in future relative to present under all scenarios is illustrated

317 in Figure 3. During the historical period, the zonally integrated, starting at of 44°S and proceeding
318 northward until 60°N, upwelling contributions to ITF transport in the Pacific Ocean steadily accumulate
319 when progressing from southern latitudes until about 20°N. Latitudes further north make little
320 contribution and accumulated upwelling is then fairly constant. This pattern changes in all future climate
321 scenario simulations. The Pacific upwelling contributions to transport volume accumulate steadily, but
322 slower with latitude than under the historical simulation, until to just north of the equator (2°N), and then,
323 after a small decrease rapidly accumulates over a few degrees of latitude. North of 20°N, the integrated
324 upwelling declines. Differences in ocean upwelling velocity under different scenarios are not significant
325 in the Pacific, except in the western boundary current region. Starting from 20°N, the wind stress in the
326 western boundary current region decreases, the upwelling of seawater weakens, (Figure 5), resulting in
327 a reduced upwelling contribution in the future scenario. Between 44°S and 15°S, the zonal cumulative
328 transport curves under SSP2-4.5 and G6solar are relatively similar. The integrated upwelling under the
329 G6sulfur scenario transitions from the smallest of the four future scenarios between 44°S and 20°S to the
330 largest a few degrees north of the equator (Figure 3).

331



332
 333 **Figure 3.** Multi-model ensemble mean zonal cumulative transport by Pacific upwelling north of 44°S
 334 during the historical simulation (1980-2014) and under the four future scenarios (2080-2100), shadings
 335 show the standard error.

336

337 **4.2 ITF by geoengineering type**

338 **4.2.1 Wind stress**

339 Godfrey et al. (1993) suggested that the Indonesian throughflow originates in the South Pacific, where
 340 the South Equatorial Current retroflects into the North Equatorial Countercurrent and enters the
 341 Indonesian Sea via the Mindanao Current. Wind stress curl is determined by the components of the wind
 342 stress vector and drives the ocean circulation (Gill and Adrian, 1982). Figure 4a shows the mean wind
 343 stress and wind stress curl in the historical period (1980-2014), and the wind stress curl is positive at low
 344 latitudes in the South Pacific, causing mass transport to the north. In the South Pacific under the SSP2-
 345 4.5 scenario during 2080-2100, the wind stress curl in the middle latitudes is stronger than in the historical
 346 period, while that at low latitudes and along the west coast of South America it is weaker than in the

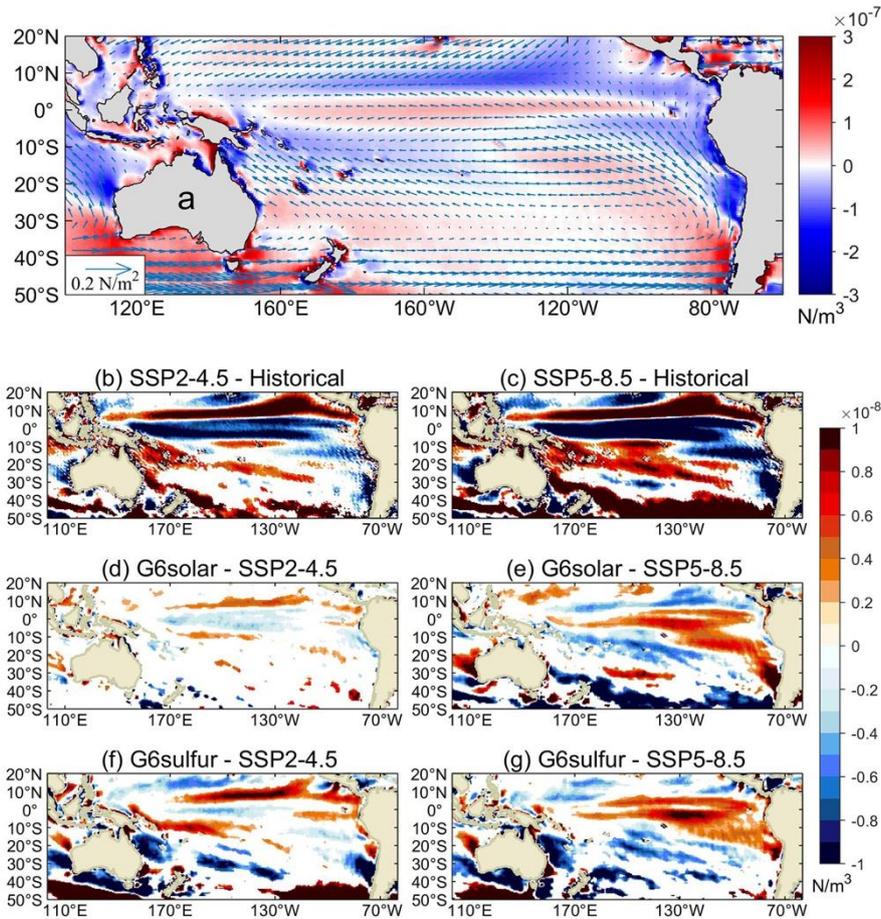
347 historical period (Figure 4a). The SSP5-8.5 scenario anomalies relative to the historical period are similar
348 but extend over a larger region and have larger amplitude (Figure 4b). Net ITF transport volume under
349 SSP5-8.5 is lower than the historical, which is consistent with the difference in wind stress curl between
350 the simulations. There is no significant difference in wind stress curl between G6solar and SSP2-4.5 in
351 mid latitudes, and the difference in low latitudes is relatively small (Figure 4c). The wind stress curl
352 under G6solar is slightly weaker at mid latitudes and slightly stronger at low latitude than with SSP5-8.5
353 (Figure 4d). Differences between wind stress curl under G6sulfur and SSP2-4.5 scenarios are mainly in
354 the mid latitudes, near the equator and the west coast of South America (Figure 4e), which are related to
355 the wind driven ITF transport changes. In contrast, the significant differences between the wind stress
356 curl under G6sulfur and SSP5-8.5 are mainly in the northeast of the South Pacific, and the wind stress
357 curl under G6sulfur is stronger than that under SSP5-8.5 (Figure 4f). The wind stress curl at the inlet of
358 the ITF is significantly weakened under the G6sulfur scenario compared with the two SSPs scenarios.

359

360

361

362



363

364 **Figure 4.** The multi-model mean differences in wind stress curl (a) the historical mean and the arrows
 365 show the wind stress, (b) SSP2-4.5 and historical, (c) SSP5-8.5 and historical, (d) G6solar and SSP2-
 366 4.5, (e) G6solar and SSP5-8.5, (f) G6sulfur and SSP2-4.5, (g) G6sulfur and SSP5-8.5. The historical
 367 period is 1980-2014, and the future scenarios period is 2080-2100. Regions where differences are not
 368 significant at the 95% level by the Wilcoxon signed-rank test are masked in white. Fig. S3 shows the
 369 ITF inlet region around the Indonesian archipelago in more detail.

370

371 The multi-model average ITF transport between G6 scenarios and SSPs scenarios shows significant
 372 differences during 2020-2100 (Table 2). Differences in wind-induced ITF transport from SSP2-4.5 are
 373 smallest with G6solar (Table 2) and are not significantly different in every ESM (Table S1). Differences
 374 between SSP5-8.5 and G6solar are the same sign for wind and upwelling forcings, contributing to larger
 375 differences in the amended island rule Wind+Upwelling transport. With G6sulfur, differences in wind
 376 and upwelling forcing differences from SSP5-8.5 are oppositely signed, and the net transport difference
 377 is quite small, but still significant for the six models ensemble (Table 2). Differences in the ITF defined

378 by buoyancy are only significant for G6sulfur-SSP5-8.5.

379

380

381 **4.2.2 Upwelling**

382 The spatial pattern of upwelling velocity at 1500 m in the Pacific under present day conditions is for
383 strong upwelling at the equator, weak upwelling in the interior, and mixed up- and down-welling along
384 the ocean boundaries (Feng et al., 2017). In future greenhouse gas climate scenarios, the main factor
385 affecting ITF transport is net upwelling in the Pacific Ocean (Feng et al., 2017; Sen Gupta et al., 2016).
386 Spatial patterns of upwelling changes are shown in Figure 5.

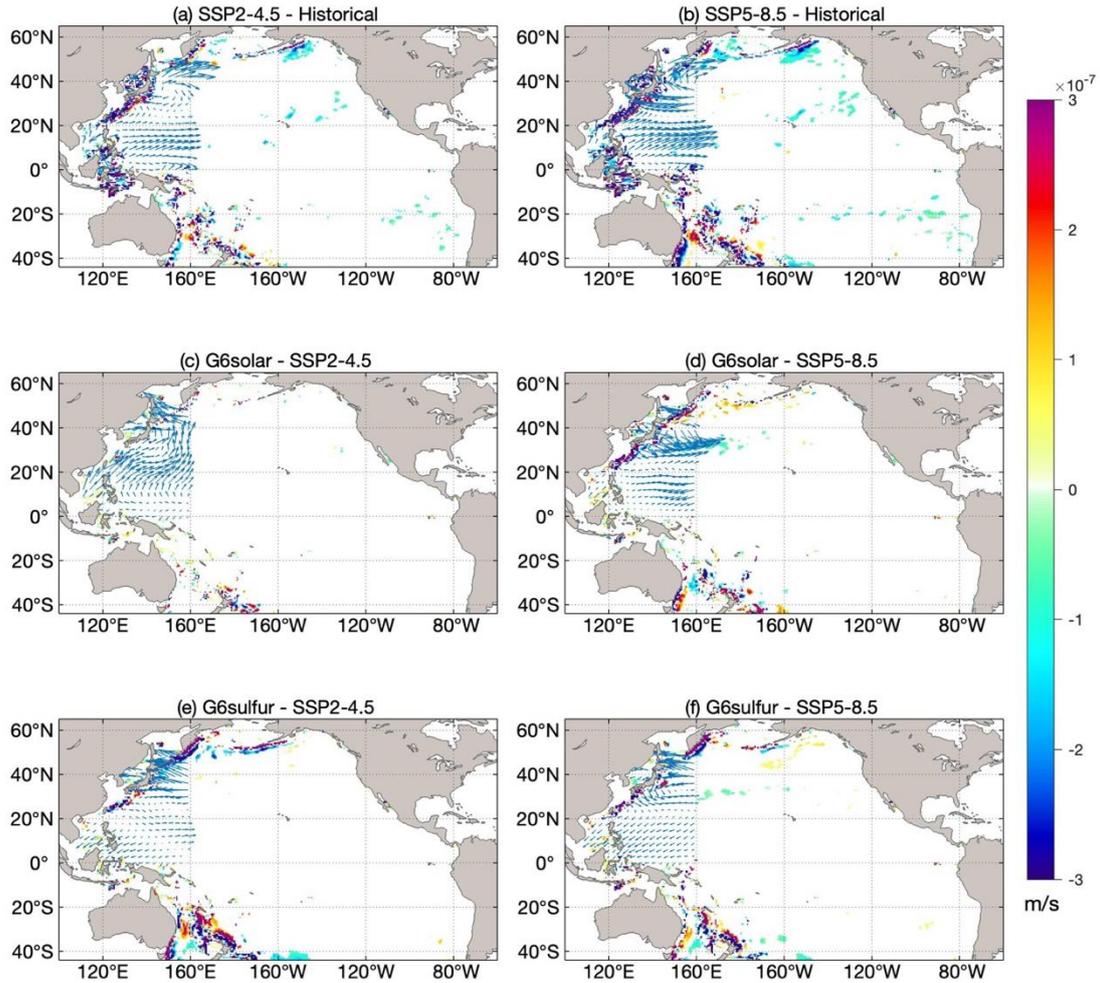
387

388 Much of the ocean shows no significant changes in upwelling velocity, but the western boundaries differ
389 significantly from the historical in both SSP scenarios (Figure 5a,b), and under SSP5-8.5 there is also a
390 significant upwelling in the equatorial eastern Pacific. The western boundary currents are an important
391 source of ITF gradient differences in wind stress that drive ocean currents (Hu et al., 2015), and these
392 gradients remain present at great depth in the western boundary current region.

393

394 The difference of upwelling velocity between G6solar and SSP2-4.5 scenarios is insignificant almost
395 everywhere (Figure 5c) once again illustrating the similarities between the solar dimming experiment
396 and its target SSP2-4.5 scenario. Differences from SSP5-8.5 are significant mainly along the extratropical
397 western ocean boundaries. The SAI experiment is clearly different from the solar dimming outcome.
398 G6sulfur differences from the SSP scenarios are clearly larger than those for G6solar and are greater in
399 the extra-tropics than in the tropics. The pattern of changes in upwelling anomalies for G6sulfur-SSP2-
400 4.5 is similar but of opposite sign to G6solar-SSP5-8.5 (Figure 5e), while differences for G6sulfur and
401 SSP5-85 are similar or slightly smaller than differences from SSP2-4.5 (Figure 5f).

402



403

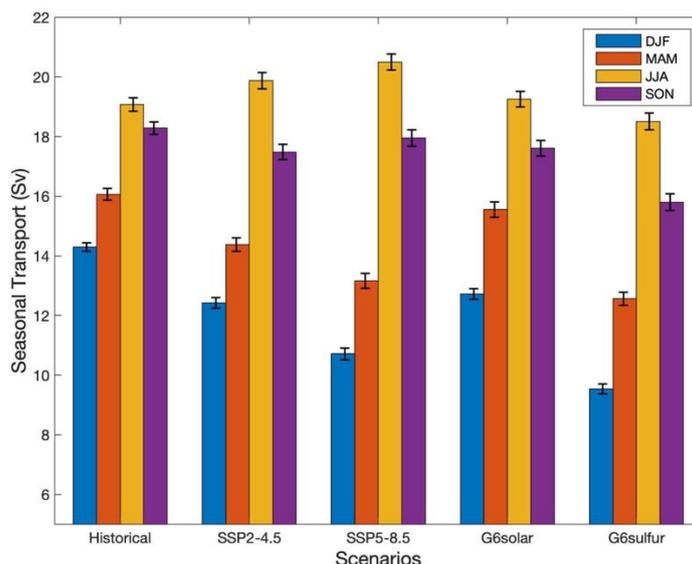
404 **Figure 5.** Changes in the multi-model ensemble mean upwelling velocity at 1500m (blue indicates
 405 increased upwelling, red indicates relative downwelling) and wind stress difference (arrow) for (a) SSP2-
 406 4.5 and historical, (b) SSP5-8.5 and historical, (c) G6solar and SSP2-4.5, (d) G6solar and SSP5-8.5, (e)
 407 G6sulfur and SSP2-4.5, (f)G6sulfur and SSP5-8.5. The historical period is 1980-2014, and the future
 408 scenarios period is 2080-2100. Regions where differences are not significant at the 95% level by the
 409 Wilcoxon signed rank test are masked in white.

410

411 4.2.3 Seasonality

412 Seasonal patterns in ITF are important and reflect changes in position of the two main precipitation
 413 convergence zones across the region. Model simulations show that decreases in ITF transport in April-
 414 May and October-November, and their recovery are due to the upper ocean changes associated with the
 415 Rossby waves in the Pacific Ocean, and that the seasonal ITF transport is closely related to wind

416 variations in the Pacific and Indian Oceans (Shinoda et al., 2012). The seasonal wind-driven ITF transport
 417 is maximum in JJA and minimum in DJF under different scenarios (Figure 6), which is consistent with
 418 the result by Wyrтки (1987). However, the differences between the G6 scenarios are largest in DJF and
 419 MAM, and these seasons are also when all 4 future scenarios are most different from the historical
 420 simulation.



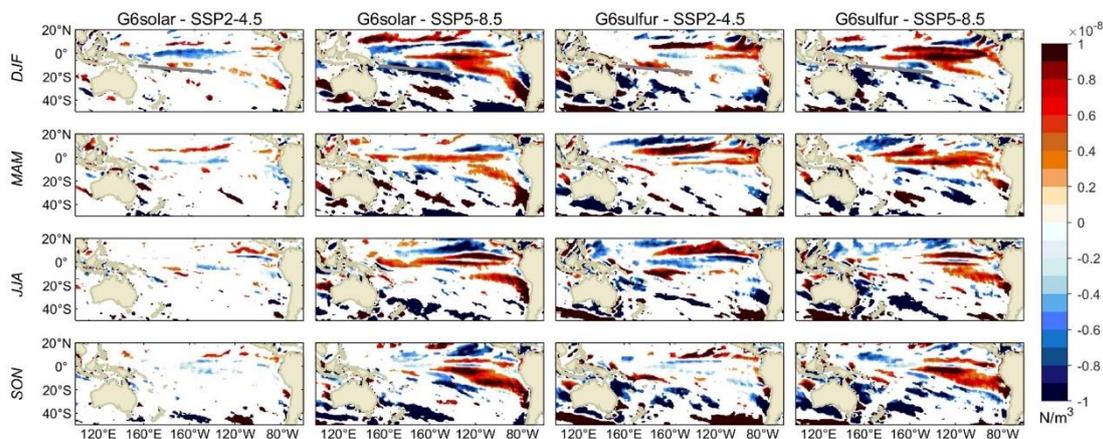
421

422 **Figure 6.** The ensemble mean seasonal wind-driven ITF transport and the standard error under the
 423 historical period (1980-2014) and future scenarios (2080-2100).

424

425 The South Pacific Convergence Zone (SPCZ) is a strong rainfall and convection zone extending from
 426 the equator to the subtropical South Pacific, which is generated by the low-level convergence between
 427 the northeast trade wind and weaker westerly wind (Vincent, 1994). The SPCZ is clearest in December-
 428 February (DJF), the Southern hemisphere summer, and is marked in the top row of Figure 7. The annual
 429 wind stress curl differences between G6solar and SSP2-4.5 are small, but the seasonal variation
 430 difference in some regions is significant. Under G6solar, compared with SSP2-4.5, the wind stress curl
 431 near the equator is weakened in DJF. In March to May (MAM), the wind stress curl in the middle and
 432 low latitudes of the southern hemisphere is generally enhanced. SSP5-8.5 has significantly lower wind
 433 stress curl in the SPCZ region relative to G6solar in DJF. In MAM, their differences are mainly in the
 434 mid latitudes. From June through November (JJA and SON), wind stress curl under SS5-8.5 is significant

435 lowered between 30 °S and 50 ° S. In contrast G6sulfur shows significant increase in the SPCZ region
 436 in DJF, and a significant decrease the south of SPCZ region in JJA relative to SSP2-4.5. There are large
 437 differences in the ocean northeast of New Zealand with the sign reversing from MAM to JJA. Differences
 438 between G6sulfur and SSP5-8.5 are not very much bigger than from SSP2-4.5, and the patterns are quite
 439 similar. The wind stress curl in the SPCZ region and its extension southeastwards is significantly
 440 weakened under G6sulfur relative to both SSP scenarios in DJF. In JJA the region with decrease in wind
 441 stress curl east from New Zealand is slightly larger relative to SSP5-8.5 and SSP2-4.5.
 442



443
 444 **Figure 7.** Seasonal ESM ensemble mean spatial differences (G6solar – SSP2-4.5, G6solar – SSP5-
 445 8.5, G6sulfur - SSP2-4.5, G6sulfur – SSP5-8.5) of the wind stress curl during 2080-2100. The white
 446 lines in each panel of the top row marks the mean the position of the South Pacific Convergence Zone
 447 (SPCZ) in DJF based on the CMIP6 multi-model mean (Brown et al., 2020). Regions where
 448 differences are not significant at the 95% level by the Wilcoxon signed rank test are masked in white,
 449 significant differences are larger than $|0.5 \times 10^{-8}| \text{ Nm}^{-3}$

450

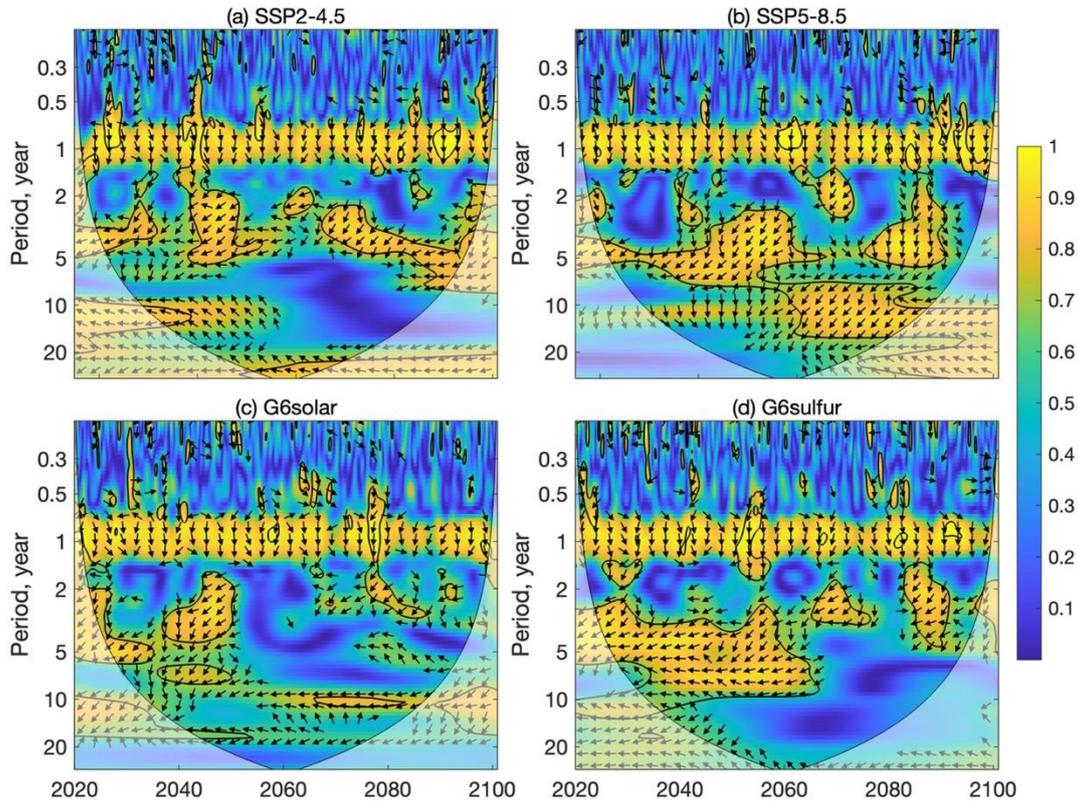
451 4.3 ITF and ENSO

452 The wind driven ITF transport estimated using the six CMIP6 models historical scenario is well within
 453 the range of 11-20 Sv, found from 22 CMIP5 models (Sen Gupta et al., 2016). These model estimates
 454 tend to slightly overestimate ITF compared with observed ITF (15 ± 3 Sv) since Godfrey’s Island Rule
 455 ignores friction due to real ocean topography (Feng et al., 2005; Wajsowicz, 1993). The rather large
 456 interannual and decadal variations in the ITF (amounting to several Sv) are mainly influenced by the

457 Pacific and Indian Ocean winds. There is an observed relationship between ITF transport and the El
458 Niño-Southern Oscillation (ENSO), with stronger transport during La Niña and weaker transport during
459 El Niña, with ITF variability lagging ENSO variability by 8-9 months (England and Huang, 2005;
460 Meyers, 1996).

461

462 We seek relationships between ITF and ENSO variability using a wavelet coherence analysis (Grinsted
463 et al., 2004) of Nino3.4 and the wind-driven ITF anomaly. This method examines correlations and phase
464 between two time series, and is useful in exploring potential causality relationships (e.g. Grinsted et al.,
465 2004; Xia et al., 2023). Since the models are not adjusted to match observations, the natural variability
466 in the oceans is not synchronized, and so a multi-model ensemble will not show useful phase relationships,
467 so instead we show just the CESM2-WACCM model in Fig. 8, and the other models in Fig. S4. Figs 8
468 and S4 show obvious annual coherence for all models as could be expected as both time series have clear
469 seasonality, but this is not actually significant against the randomized phase Fourier background
470 hypothesis. There are multi-year significant power episodes in all models, though there are no significant
471 differences in power between the scenarios at any band between annual and decadal. The two appear in
472 anti-phase (Figure 8) in line with observed stronger transport during La Niña and weaker transport during
473 El Niña. At the same time, ITF variability also lags behind ENSO on the whole, but there are differences
474 among different models.



475

476 **Figure 8.** The squared wavelet coherence between the Nino3.4 (representing ENSO) and the wind-
 477 driven ITF transport monthly anomalies under the two SSPs (2015-2100) and two G6 (2020-2100)
 478 scenarios in CESM2-WACCM model. The 95% significance level above the background of 1000
 479 Monte-Carlo ensemble of series of identical mean and standard deviation with identical power spectra
 480 but phase-randomized Fourier noise (chosen instead of the usual first order autoregressive null
 481 hypothesis here because of the strong annual signal; Xia et al. (2023)), is represented by a thick contour
 482 line. The arrows indicate the relative phase relationship, that is, in-phase points to the right, anti-phase
 483 points to the left, the arrow up indicates that the ITF anomaly leads ENSO by 90° , and a down arrow
 484 indicates that the ITF anomaly lags ENSO by 90° . The other models are shown in Fig. S4.

485 5. Summary and Discussion

486 The six ESM we use concur on weakening of ITF transport in all future scenarios. That is SRM cannot
 487 restore the ITF to its historic levels (Table 2, Fig 2). This contrasts somewhat to the changes simulated
 488 in the AMOC under SRM with GHG forcing, where it seems that SRM can partly reverse the slow down
 489 in AMOC induced by GHG forcing, reducing impacts from around 35% to 24% (Muri et al., 2018; Tilmes
 490 et al., 2020; Xie et al., 2022). This illustrates the important regional variability in responses to SRM.

491

492 Weakening of the ITF transport appears in all future scenarios, both with pure GHG forcing, and

493 combining GHG and SRM strategies. The ITF transport changes are defined almost totally (around 90%)
494 by significant differences in Pacific upwelling (Figure 2a and 2b). This is consistent with the conclusion
495 that the weakening trend of ITF under global warming predicted by high-precision ocean models is not
496 directly related to the change of Pacific trade winds but to the reduction of Pacific deep-sea upwelling
497 (Feng et al., 2017). On centennial scales, the decrease of the net deep ocean upwelling in the tropics and
498 the South Pacific, especially the changes in the western boundary current system is what determines ITF
499 transport. Buoyancy forcing can only estimate the interannual variation of the ITF, and our study
500 supports the utility of the Amended Island Rule in estimating centennial changes in ITF transport. The
501 Island rule was specifically formulated considering the difficulties in measuring flow in complex
502 topography. Instead, the Sverdrup theory of wind forcing was utilized, allowing much larger scale
503 observations to provide useful estimates of ITF. This methodology should also be suitable for the global
504 models we have analysed here. This contrasts with the relatively small regions of the DBP (Fig. 1), that
505 may not be consistently captured in the global models we analyze.

506

507 Sen Gupta et al. (2021) note that projected weakening of the ITF and differences between ESM can be
508 explained by changes in large-scale surface winds. This contrasts with our findings where changes in
509 wind driven transport are not significantly different between models, but instead upwelling in the
510 extratropical western boundary zones dominates changes between scenarios. However, western boundary
511 currents are deep and narrow and differ from the shallow and wide eastern boundary currents. The tropics
512 experience weaker (and reversed) trade winds from those that dominate the extratropical regions. The
513 geographical differences in upwelling suggest that wind changes are driving the overall changes in ITF
514 via upwelling regions, and so in effect supporting the conclusion of Sen Gupta et al. (2021) that
515 differences in future surface winds explain most of the differences in future large scale current systems.

516

517 SSP2-4.5 global radiative forcing was the design target of the G6 experiments despite GHG
518 concentrations being at SSP5-8.5 levels. The difference in wind stress curl between G6solar and SSP2-
519 4.5 indicates that the SD experiment performs better at reversing GHG induced changes in Pacific wind
520 than G6sulfur. The G6sulfur SAI experiment leads to a significant change in the winds in mid and low

521 latitude Pacific Ocean, which results in even lower estimated ITF transport than under the high GHG
522 SSP5-8.5 forcing alone. Furthermore, G6sulfur also impacts deep ocean upwelling especially in the
523 extratropical western boundary current region, such that the ITF transport during the 21st century under
524 the G6sulfur scenario is slower than that under the G6solar scenario. The G6 scenarios do not affect low
525 latitude western boundary currents and upwelling, for example the upwelling near the Mindanao current
526 is unaffected while the upwelling along the Kuroshio current is apparently displaced in both G6
527 experiments. The ITF transport under the SD experiment was stronger than under the SAI experiment
528 and even higher than its target SSP2-4.5 scenario level at the end of the 21st century.

529

530 Changes in circulation in the future will have important impacts on aquatic ecology and fisheries (Dubois
531 et al., 2016). In fact, the population in Indonesia's coastal areas, especially those in the islands through
532 which the ITF passes, are highly dependent on fisheries and hence, the changes in ITF under both pure
533 GHG and mixed GHG and SRM scenarios will have important local implications on the livelihood and
534 ways of life of the local populations. Seasonal variations in ITF transport reflect important processes in
535 the tropical convergence zones, and these are clearly impacted by all 4 future scenarios in generally subtle
536 ways. But the largest differences are seen between the two most challenging scenarios to simulate –
537 SSP5-8.5 and G6sulfur. Despite the large size of perturbation that these forcings apply in the simulations,
538 and the differences between climate models in parameterizing the SAI schemes, the finding are rather
539 robust in the changes of winds in all seasons in the Pacific Ocean and Maritime Continent.

540

541 SAI is a far more feasible method of SRM than SD (Shepherd, 2009), but it produces far larger
542 differences in various climate fields from GHG and historic simulations than does SD (Visioni et al.,
543 2021), and far larger across-ESM differences as the models process the aerosol impacts in varied ways
544 (Visioni et al., 2021). The differences in winds noted in G6sulfur likely arise from differences in
545 stratospheric heating due to the sulfur aerosols that then drive tropospheric circulation changes (Visioni
546 et al., 2020).

547

548 Although ESM can provide reliable predictions of the ITF transport, the accuracy of global meso- and

549 small-scale spatial and seasonal changes remains an issue. These relatively small-scale differences are
550 potentially more important for local impacts than differences in larger scale or annual changes. These
551 aspects will need to be explored using impact models tailored to the region, ideally through initiatives
552 focused on the Global South like the Degrees Initiative (<https://www.degrees.ngo/>) and addressing
553 concerns raised by local rightsholders.

554

555 **Code and data availability**

556 All model data used in this work are available from the Earth System Grid Federation (WCRP, 2022;
557 <https://esgf-node.llnl.gov/projects/cmip6>, last access: 3 July 2022).

558 **Author contributions**

559 JCM conceived and designed the analysis. CS collected the data and performed the analysis. CS and
560 JCM wrote the paper. All authors contributed to the discussion.

561 **Competing interests**

562 The contact author has declared that neither they nor their co-authors have any competing interests.

563 **Financial support**

564 This research has been supported by the National Key Research and Development Program of China
565 (grant nos. 2021YFB3900105), State Key Laboratory of Earth Surface Processes and Resource Ecology
566 (2022-ZD-05) and Finnish Academy COLD Consortium (grant no. 322430).

567

568 **Reference**

569 Alory, G., Wijffels, S., and Meyers, G.: Observed temperature trends in the Indian Ocean over 1960–
570 1999 and associated mechanisms, *Geophys. Res. Lett.*, 34,
571 <https://doi.org/10.1029/2006gl028044>, 2007.

572 Amante, C., and Eakins, B. W.: ETOPO1 arc-minute global relief model: procedures, data sources and
573 analysis, NOAA Tech. Memo. NESDIS NGDC-24, <https://doi.org/10.7289/V5C8276M>, 2009.

574 Andersson, H. C., and Stigebrandt, A.: Regulation of the Indonesian throughflow by baroclinic draining
575 of the North Australian Basin, *Deep Sea Res., Part I*, 52, 2214-2233,
576 <https://doi.org/10.1016/j.dsr.2005.06.014>, 2005.

577 Ayers, J. M., Strutton, P. G., Coles, V. J., Hood, R. R., and Matear, R. J.: Indonesian throughflow nutrient
578 fluxes and their potential impact on Indian Ocean productivity, *Geophys. Res. Lett.*, 41, 5060-
579 5067, <https://doi.org/10.1002/2014gl060593>, 2014.

580 Boucher, O., Servonnat, J., Albright, A. L., Aumont, O., Balkanski, Y., Bastrikov, V., Bekki, S., Bonnet,

581 R., Bony, S., Bopp, L., Braconnot, P., Brockmann, P., Cadule, P., Caubel, A., Cheruy, F., Codron,
582 F., Cozic, A., Cugnet, D., D'Andrea, F., Davini, P., Lavergne, C., Denvil, S., Deshayes, J.,
583 Devilliers, M., Ducharne, A., Dufresne, J. L., Dupont, E., Éthé, C., Fairhead, L., Falletti, L.,
584 Flavoni, S., Foujols, M. A., Gardoll, S., Gastineau, G., Ghattas, J., Grandpeix, J. Y., Guenet, B.,
585 Guez, L. E., Guilyardi, E., Guimberteau, M., Hauglustaine, D., Hourdin, F., Idelkadi, A.,
586 Joussaume, S., Kageyama, M., Khodri, M., Krinner, G., Lebas, N., Levvasseur, G., Lévy, C.,
587 Li, L., Lott, F., Lurton, T., Luysaert, S., Madec, G., Madeleine, J. B., Maignan, F., Marchand,
588 M., Marti, O., Mellul, L., Meurdesoif, Y., Mignot, J., Musat, I., Ottlé, C., Peylin, P., Planton, Y.,
589 Polcher, J., Rio, C., Rochetin, N., Rousset, C., Sepulchre, P., Sima, A., Swingedouw, D., Thié
590 blemont, R., Traore, A. K., Vancoppenolle, M., Vial, J., Vialard, J., Viovy, N., and Vuichard, N.:
591 Presentation and Evaluation of the IPSL-CM6A-LR Climate Model, *J. Adv. Model. Earth Syst.*,
592 12, <https://doi.org/10.1029/2019ms002010>, 2020.

593 Cheng, W., MacMartin, D. G., Kravitz, B., Visoni, D., Bednarz, E. M., Xu, Y., Luo, Y., Huang, L., Hu,
594 Y., Staten, P. W., Hitchcock, P., Moore, J. C., Guo, A., and Deng, X.: Changes in Hadley
595 circulation and intertropical convergence zone under strategic stratospheric aerosol
596 geoengineering, *npj Clim. Atmos. Sci.*, 5, <https://doi.org/10.1038/s41612-022-00254-6>, 2022.

597 Clarke, A. J., and Liu, X.: Interannual sea level in the northern and eastern Indian Ocean, *J. Phys.*
598 *Oceanogr.*, 24, 1224-1235, [https://doi.org/10.1175/1520-0485\(1994\)024<1224:ISLITN>2.0.CO;2](https://doi.org/10.1175/1520-0485(1994)024<1224:ISLITN>2.0.CO;2), 1994.

600 Danabasoglu, G., Lamarque, J. F., Bacmeister, J., Bailey, D. A., DuVivier, A. K., Edwards, J., Emmons,
601 L. K., Fasullo, J., Garcia, R., Gettelman, A., Hannay, C., Holland, M. M., Large, W. G.,
602 Lauritzen, P. H., Lawrence, D. M., Lenaerts, J. T. M., Lindsay, K., Lipscomb, W. H., Mills, M.
603 J., Neale, R., Oleson, K. W., Otto-Bliesner, B., Phillips, A. S., Sacks, W., Tilmes, S.,
604 Kampenhout, L., Vertenstein, M., Bertini, A., Dennis, J., Deser, C., Fischer, C., Fox-Kemper,
605 B., Kay, J. E., Kinnison, D., Kushner, P. J., Larson, V. E., Long, M. C., Mickelson, S., Moore,
606 J. K., Nienhouse, E., Polvani, L., Rasch, P. J., and Strand, W. G.: The Community Earth System
607 Model Version 2 (CESM2), *J. Adv. Model. Earth Syst.*, 12,
608 <https://doi.org/10.1029/2019ms001916>, 2020.

609 Duan, J., Chen, Z., and Wu, L.: Projected changes of the low-latitude north-western Pacific wind-driven
610 circulation under global warming, *Geophys. Res. Lett.*, 44, 4976-4984,
611 <https://doi.org/10.1002/2017gl073355>, 2017.

612 Dubois, M., Rossi, V., Ser-Giacomi, E., Arnaud-Haond, S., López, C., and Hernández-García, E.: Linking
613 basin-scale connectivity, oceanography and population dynamics for the conservation and
614 management of marine ecosystems, *Global Ecol. Biogeogr.*, 25, 503-515,
615 <https://doi.org/10.1111/geb.12431>, 2016.

616 Durgadoo, J. V., Rühs, S., Biastoch, A., and Böning, C. W. B.: Indian Ocean sources of Agulhas leakage,
617 *J. Geophys. Res.: Oceans*, 122, 3481-3499, <https://doi.org/10.1002/2016jc012676>, 2017.

618 England, M. H., and Huang, F.: On the interannual variability of the Indonesian Throughflow and its
619 linkage with ENSO, *J. Clim.*, 18, 1435-1444, <https://doi.org/10.1175/JCLI3322.1>, 2005.

620 Eyring, V., Bony, S., Meehl, G. A., Senior, C. A., Stevens, B., Stouffer, R. J., and Taylor, K. E.: Overview
621 of the Coupled Model Intercomparison Project Phase 6 (CMIP6) experimental design and
622 organization, *Geosci. Model Dev.*, 9, 1937-1958, <https://doi.org/10.5194/gmd-9-1937-2016>,

623 2016.

624 Feng, M., Böning, C., Biastoch, A., Behrens, E., Weller, E., and Masumoto, Y.: The reversal of the multi-
625 decadal trends of the equatorial Pacific easterly winds, and the Indonesian Throughflow and
626 Leeuwin Current transports, *Geophys. Res. Lett.*, 38, L11604,
627 <https://doi.org/10.1029/2011gl047291>, 2011.

628 Feng, M., Sun, C., Matear, R. J., Chamberlain, M. A., Craig, P., Ridgway, K. R., and Schiller, A.: Marine
629 Downscaling of a Future Climate Scenario for Australian Boundary Currents, *J. Clim.*, 25, 2947-
630 2962, <https://doi.org/10.1175/jcli-d-11-00159.1>, 2012.

631 Feng, M., Wijffels, S., Godfrey, S., and Meyers, G.: Do eddies play a role in the momentum balance of
632 the Leeuwin Current?, *J. Phys. Oceanogr.*, 35, 964-975, <https://doi.org/10.1175/JPO2730.1>,
633 2005.

634 Feng, M., Zhang, X., Sloyan, B., and Chamberlain, M.: Contribution of the deep ocean to the centennial
635 changes of the Indonesian Throughflow, *Geophys. Res. Lett.*, 44, 2859-2867,
636 <https://doi.org/10.1002/2017gl072577>, 2017.

637 Gertler, C. G., O'Gorman, P. A., Kravitz, B., Moore, J. C., Phipps, S. J., and Watanabe, S.: Weakening of
638 the Extratropical Storm Tracks in Solar Geoengineering Scenarios, *Geophys. Res. Lett.*, 47,
639 <https://doi.org/10.1029/2020gl087348>, 2020.

640 Gill, A. E., and Adrian, E.: *Atmosphere-ocean dynamics*: Academic press, 30 pp., ISBN0122835220,
641 1982.

642 Godfrey, J., Wilkin, J., and Hirst, A.: Why does the Indonesian Throughflow appear to originate from the
643 North Pacific?, *J. Phys. Oceanogr.*, 23, 1087-1098, [https://doi.org/10.1175/1520-0485\(1993\)023%3C1087:WDTITA%3E2.0.CO;2](https://doi.org/10.1175/1520-0485(1993)023%3C1087:WDTITA%3E2.0.CO;2), 1993.

645 Godfrey, J. S.: A sverdrup model of the depth-integrated flow for the world ocean allowing for island
646 circulations, *Geophys. Astrophys. Fluid Dyn.*, 45, 89-112,
647 <https://doi.org/10.1080/03091928908208894>, 1989.

648 Godfrey, J. S.: The effect of the Indonesian throughflow on ocean circulation and heat exchange with the
649 atmosphere: A review, *J. Geophys. Res.: Oceans*, 101, 12217-12237,
650 <https://doi.org/10.1029/95jc03860>, 1996.

651 Gordon, A. L.: Inter-ocean exchange of thermocline water, *J. Geophys. Res.: Oceans*, 91, 5037-5046,
652 <https://doi.org/10.1029/JC091iC04p05037>, 1986.

653 Gordon, A. L.: The Indonesian Seas, *Oceanogr.*, 18, 14, <https://doi.org/10.5670/oceanog.2005.01>, 2005.

654 Gordon, A. L., Susanto, R. D., and Field, A.: Throughflow within Makassar Strait, *Geophys. Res. Lett.*,
655 26, 3325-3328, <https://doi.org/10.1029/1999GL002340>, 1999.

656 Gorgues, T., Menkes, C., Aumont, O., Dandonneau, Y., Madec, G., and Rodgers, K.: Indonesian
657 throughflow control of the eastern equatorial Pacific biogeochemistry, *Geophys. Res. Lett.*, 34,
658 <https://doi.org/10.1029/2006gl028210>, 2007.

659 Guo, A., Moore, J. C., and Ji, D.: Tropical atmospheric circulation response to the G1 sunshade
660 geoengineering radiative forcing experiment, *Atmos. Chem. Phys.*, 18, 8689-8706,
661 <https://doi.org/10.5194/acp-18-8689-2018>, 2018.

662 Hirst, A. C., and Godfrey, J.: The response to a sudden change in Indonesian throughflow in a global
663 ocean GCM, *J. Phys. Oceanogr.*, 24, 1895-1910, [https://doi.org/10.1175/1520-0485\(1994\)024<1895:TRTASC>2.0.CO;2](https://doi.org/10.1175/1520-0485(1994)024<1895:TRTASC>2.0.CO;2), 1994.

665 Hong, Y., Moore, J. C., Jevrejeva, S., Ji, D., Phipps, S. J., Lenton, A., Tilmes, S., Watanabe, S., and Zhao,
666 L.: Impact of the GeoMIP G1 sunshade geoengineering experiment on the Atlantic meridional
667 overturning circulation, *Environ. Res. Lett.*, 12, <https://doi.org/10.1088/1748-9326/aa5fb8>,
668 2017.

669 Hu, D., Wu, L., Cai, W., Gupta, A. S., Ganachaud, A., Qiu, B., Gordon, A. L., Lin, X., Chen, Z., Hu, S.,
670 Wang, G., Wang, Q., Sprintall, J., Qu, T., Kashino, Y., Wang, F., and Kessler, W. S.: Pacific
671 western boundary currents and their roles in climate, *Nat.*, 522, 299-308,
672 <https://doi.org/10.1038/nature14504>, 2015.

673 Hu, S., and Sprintall, J.: Interannual variability of the Indonesian Throughflow: The salinity effect, *J.*
674 *Geophys. Res.: Oceans*, 121, 2596-2615, <https://doi.org/10.1002/2015jc011495>, 2016.

675 Kravitz, B., Robock, A., Tilmes, S., Boucher, O., English, J. M., Irvine, P. J., Jones, A., Lawrence, M. G.,
676 MacCracken, M., Muri, H., Moore, J. C., Niemeier, U., Phipps, S. J., Sillmann, J., Storelvmo,
677 T., Wang, H., and Watanabe, S.: The Geoengineering Model Intercomparison Project Phase 6
678 (GeoMIP6): simulation design and preliminary results, *Geosci. Model Dev.*, 8, 3379-3392,
679 <https://doi.org/10.5194/gmd-8-3379-2015>, 2015.

680 Kriegler, E., O'Neill, B. C., Hallegatte, S., Kram, T., Lempert, R. J., Moss, R. H., and Wilbanks, T.: The
681 need for and use of socio-economic scenarios for climate change analysis: A new approach
682 based on shared socio-economic pathways, *Global Environ. Change*, 22, 807-822,
683 <https://doi.org/10.1016/j.gloenvcha.2012.05.005>, 2012.

684 Lee, T., Fukumori, I., Menemenlis, D., Xing, Z., and Fu, L.-L.: Effects of the Indonesian throughflow on
685 the Pacific and Indian Oceans, *J. Phys. Oceanogr.*, 32, 1404-1429, [https://doi.org/10.1175/1520-0485\(2002\)032<1404:EOTITO>2.0.CO;2](https://doi.org/10.1175/1520-0485(2002)032<1404:EOTITO>2.0.CO;2), 2002.

687 Lukas, R., Yamagata, T., and McCreary, J. P.: Pacific low-latitude western boundary currents and the
688 Indonesian throughflow, *J. Geophys. Res.: Oceans*, 101, 12209-12216,
689 <https://doi.org/10.1029/96jc01204>, 1996.

690 MacMartin, D. G., and Kravitz, B.: Dynamic climate emulators for solar geoengineering, *Atmos. Chem.*
691 *Phys.*, 16, 15789-15799, <https://doi.org/10.5194/acp-16-15789-2016>, 2016.

692 Mauritsen, T., Bader, J., Becker, T., Behrens, J., Bittner, M., Brokopf, R., Brovkin, V., Claussen, M.,
693 Crueger, T., Esch, M., Fast, I., Fiedler, S., Flaschner, D., Gayler, V., Giorgetta, M., Goll, D. S.,
694 Haak, H., Hagemann, S., Hedemann, C., Hohenegger, C., Ilyina, T., Jahns, T., Jimenez-de-la-
695 Cuesta, D., Jungclaus, J., Kleinen, T., Kloster, S., Kracher, D., Kinne, S., Kleberg, D., Lasslop,
696 G., Kornblueh, L., Marotzke, J., Matei, D., Meraner, K., Mikolajewicz, U., Modali, K., Mobis,
697 B., Muller, W. A., Nabel, J., Nam, C. C. W., Notz, D., Nyawira, S. S., Paulsen, H., Peters, K.,
698 Pincus, R., Pohlmann, H., Pongratz, J., Popp, M., Raddatz, T. J., Rast, S., Redler, R., Reick, C.
699 H., Rohrschneider, T., Schemann, V., Schmidt, H., Schnur, R., Schulzweida, U., Six, K. D., Stein,
700 L., Stemmler, I., Stevens, B., von Storch, J. S., Tian, F., Voigt, A., Vrese, P., Wieners, K. H.,
701 Wilkenskjaeld, S., Winkler, A., and Roeckner, E.: Developments in the MPI-M Earth System
702 Model version 1.2 (MPI-ESM1.2) and Its Response to Increasing CO₂, *J. Adv. Model. Earth*
703 *Syst.*, 11, 998-1038, <https://doi.org/10.1029/2018MS001400>, 2019.

704 Meyers, G.: Variation of Indonesian throughflow and the El Niño-southern oscillation, *J. Geophys. Res.:*
705 *Oceans*, 101, 12255-12263, <https://doi.org/10.1029/95JC03729>, 1996.

706 Moore, J. C., Grinsted, A., Guo, X., Yu, X., Jevrejeva, S., Rinke, A., Cui, X., Kravitz, B., Lenton, A.,

707 Watanabe, S., and Ji, D.: Atlantic hurricane surge response to geoengineering, *Proc. Natl. Acad.*
708 *Sci. U. S. A.*, 112, 13794-13799, <https://doi.org/10.1073/pnas.1510530112>, 2015.

709 Moore, J. C., Yue, C., Zhao, L., Guo, X., Watanabe, S., and Ji, D.: Greenland Ice Sheet Response to
710 Stratospheric Aerosol Injection Geoengineering, *Earth. Fut.*, 7, 1451-1463,
711 <https://doi.org/10.1029/2019EF001393>, 2019.

712 Muri, H., Tjiputra, J., Otterå, O. H., Adakudlu, M., Lauvset, S. K., Grini, A., Schulz, M., Niemeier, U.,
713 and Kristjánsson, J. E.: Climate Response to Aerosol Geoengineering: A Multimethod
714 Comparison, *J. Clim.*, 31, 6319-6340, <https://doi.org/10.1175/jcli-d-17-0620.1>, 2018.

715 O'Neill, B. C., Tebaldi, C., Vuuren, D. P. v., Eyring, V., Friedlingstein, P., Hurtt, G., Knutti, R., Kriegler,
716 E., Lamarque, J.-F., and Lowe, J.: The scenario model intercomparison project (ScenarioMIP)
717 for CMIP6, *Geosci. Model Dev.*, 9, 3461-3482, <https://doi.org/10.5194/gmd-9-3461-2016>, 2016.

718 Potemra, J. T., Lukas, R., and Mitchum, G. T.: Large-scale estimation of transport from the Pacific to the
719 Indian Ocean, *J. Geophys. Res.: Oceans*, 102, 27795-27812, <https://doi.org/10.1029/97jc01719>,
720 1997.

721 Séférian, R., Nabat, P., Michou, M., Saint-Martin, D., Voltaire, A., Colin, J., Decharme, B., Delire, C.,
722 Berthet, S., Chevallier, M., Sénési, S., Franchisteguy, L., Vial, J., Mallet, M., Joetzjer, E.,
723 Geoffroy, O., Guérémy, J. F., Moine, M. P., Msadek, R., Ribes, A., Rocher, M., Roehrig, R.,
724 Salas-y-Méllia, D., Sanchez, E., Terray, L., Valecke, S., Waldman, R., Aumont, O., Bopp, L.,
725 Deshayes, J., Éthé, C., and Madec, G.: Evaluation of CNRM Earth System Model, CNRM-
726 *ESM2-1: Role of Earth System Processes in Present-Day and Future Climate*, *J. Adv. Model.*
727 *Earth Syst.*, 11, 4182-4227, <https://doi.org/10.1029/2019ms001791>, 2019.

728 Sellar, A. A., Jones, C. G., Mulcahy, J. P., Tang, Y., Yool, A., Wiltshire, A., O'Connor, F. M., Stringer, M.,
729 Hill, R., Palmieri, J., Woodward, S., Mora, L., Kuhlbrodt, T., Rumbold, S. T., Kelley, D. I., Ellis,
730 R., Johnson, C. E., Walton, J., Abraham, N. L., Andrews, M. B., Andrews, T., Archibald, A. T.,
731 Berthou, S., Burke, E., Blockley, E., Carslaw, K., Dalvi, M., Edwards, J., Folberth, G. A.,
732 Gedney, N., Griffiths, P. T., Harper, A. B., Hendry, M. A., Hewitt, A. J., Johnson, B., Jones, A.,
733 Jones, C. D., Keeble, J., Liddicoat, S., Morgenstern, O., Parker, R. J., Predoi, V., Robertson, E.,
734 Siahann, A., Smith, R. S., Swaminathan, R., Woodhouse, M. T., Zeng, G., and Zerroukat, M.:
735 *UKESM1: Description and Evaluation of the U.K. Earth System Model*, *J. Adv. Model. Earth*
736 *Syst.*, 11, 4513-4558, <https://doi.org/10.1029/2019ms001739>, 2019.

737 Sen Gupta, A., Ganachaud, A., McGregor, S., Brown, J. N., and Muir, L.: Drivers of the projected
738 changes to the Pacific Ocean equatorial circulation, *Geophys. Res. Lett.*, 39, L09605,
739 <https://doi.org/10.1029/2012gl051447>, 2012.

740 Sen Gupta, A., McGregor, S., Sebille, E., Ganachaud, A., Brown, J. N., and Santoso, A.: Future changes
741 to the Indonesian Throughflow and Pacific circulation: The differing role of wind and deep
742 circulation changes, *Geophys. Res. Lett.*, 43, 1669-1678, <https://doi.org/10.1002/2016gl067757>,
743 2016.

744 Sen Gupta, A., Stellema, A., Pontes, G. M., Taschetto, A. S., Verges, A., and Rossi, V.: Future changes to
745 the upper ocean Western Boundary Currents across two generations of climate models, *Sci. Rep.*,
746 11, 9538, <https://doi.org/10.1038/s41598-021-88934-w>, 2021.

747 Shepherd, J. G.: *Geoengineering the climate: science, governance and uncertainty*: Royal Society,
748 London, 98 pp., ISBN085403773X, 2009.

749 Shinoda, T., Han, W., Metzger, E. J., and Hurlburt, H. E.: Seasonal Variation of the Indonesian
750 Throughflow in Makassar Strait, *J. Phys. Oceanogr.*, 42, 1099-1123,
751 <https://doi.org/10.1175/jpo-d-11-0120.1>, 2012.

752 Smyth, J. E., Russotto, R. D., and Storelvmo, T.: Thermodynamic and dynamic responses of the
753 hydrological cycle to solar dimming, *Atmos. Chem. Phys.*, 17, 6439-6453,
754 <https://doi.org/10.5194/acp-17-6439-2017>, 2017.

755 Sprintall, J., Wijffels, S. E., Molcard, R., and Jaya, I.: Direct estimates of the Indonesian Throughflow
756 entering the Indian Ocean: 2004–2006, *J. Geophys. Res.*, 114,
757 <https://doi.org/10.1029/2008jc005257>, 2009.

758 Staten, P. W., Grise, K. M., Davis, S. M., Karnauskas, K., and Davis, N.: Regional Widening of Tropical
759 Overturning: Forced Change, Natural Variability, and Recent Trends, *J. Geophys. Res.: Atmos.*,
760 124, 6104-6119, <https://doi.org/10.1029/2018JD030100>, 2019.

761 Stigebrandt, A.: The North Pacific: A global-scale estuary, *J. Phys. Oceanogr.*, 14, 464-470,
762 [https://doi.org/10.1175/1520-0485\(1984\)014<0464:TNPAGS>2.0.CO;2](https://doi.org/10.1175/1520-0485(1984)014<0464:TNPAGS>2.0.CO;2), 1984.

763 Susanto, R. D., and Song, Y. T.: Indonesian throughflow proxy from satellite altimeters and gravimeters,
764 *J. Geophys. Res.: Oceans*, 120, 2844-2855, <https://doi.org/10.1002/2014jc010382>, 2015.

765 Sverdrup, H. U.: Wind-driven currents in a baroclinic ocean; with application to the equatorial currents
766 of the eastern Pacific, *Proc. Natl. Acad. Sci. U. S. A.*, 33, 318,
767 <https://doi.org/10.1073/pnas.33.11.318>, 1947.

768 Talley, L. D.: Freshwater transport estimates and the global overturning circulation: Shallow, deep and
769 throughflow components, *Prog. Oceanogr.*, 78, 257-303,
770 <https://doi.org/10.1016/j.pocean.2008.05.001>, 2008.

771 Tilmes, S., MacMartin, D. G., Lenaerts, J. T. M., van Kampenhout, L., Muntjewerf, L., Xia, L., Harrison,
772 C. S., Krumhardt, K. M., Mills, M. J., Kravitz, B., and Robock, A.: Reaching 1.5 and 2.0 °C
773 global surface temperature targets using stratospheric aerosol geoengineering, *Earth Syst.*
774 *Dynam.*, 11, 579-601, <https://doi.org/10.5194/esd-11-579-2020>, 2020.

775 van Vuuren, D. P., Edmonds, J., Kainuma, M., Riahi, K., Thomson, A., Hibbard, K., Hurtt, G. C., Kram,
776 T., Krey, V., Lamarque, J.-F., Masui, T., Meinshausen, M., Nakicenovic, N., Smith, S. J., and
777 Rose, S. K.: The representative concentration pathways: an overview, *Clim. Change*, 109, 5-31,
778 <https://doi.org/10.1007/s10584-011-0148-z>, 2011.

779 Vecchi, G. A., and Soden, B. J.: Global Warming and the Weakening of the Tropical Circulation, *J. Clim.*,
780 20, 4316-4340, <https://doi.org/10.1175/jcli4258.1>, 2007.

781 Vincent, D. G.: The South Pacific convergence zone (SPCZ): A review, *Mon. Weather Rev.*, 122, 1949-
782 1970, [https://doi.org/10.1175/1520-0493\(1994\)122<1949:TSPCZA>2.0.CO;2](https://doi.org/10.1175/1520-0493(1994)122<1949:TSPCZA>2.0.CO;2), 1994.

783 Visioni, D., MacMartin, D. G., Kravitz, B., Boucher, O., Jones, A., Lurton, T., Martine, M., Mills, M. J.,
784 Nabat, P., Niemeier, U., Séférian, R., and Tilmes, S.: Identifying the sources of uncertainty in
785 climate model simulations of solar radiation modification with the G6sulfur and G6solar
786 Geoengineering Model Intercomparison Project (GeoMIP) simulations, *Atmos. Chem. Phys.*,
787 21, 10039-10063, <https://doi.org/10.5194/acp-21-10039-2021>, 2021.

788 Visioni, D., MacMartin, D. G., Kravitz, B., Lee, W., Simpson, I. R., and Richter, J. H.: Reduced Poleward
789 Transport Due to Stratospheric Heating Under Stratospheric Aerosols Geoengineering, *Geophys.*
790 *Res. Lett.*, 47, <https://doi.org/10.1029/2020gl089470>, 2020.

791 Wajsowicz, R. C.: The circulation of the depth-integrated flow around an island with application to the
792 Indonesian Throughflow, *J. Phys. Oceanogr.*, 23, 1470-1484, [https://doi.org/10.1175/1520-0485\(1993\)023<1470:TCOTDI>2.0.CO;2](https://doi.org/10.1175/1520-0485(1993)023<1470:TCOTDI>2.0.CO;2), 1993.
793
794 Wang, Q., Moore, J. C., and Ji, D.: A statistical examination of the effects of stratospheric sulfate
795 geoengineering on tropical storm genesis, *Atmos. Chem. Phys.*, 18, 9173-9188,
796 <https://doi.org/10.5194/acp-18-9173-2018>, 2018.
797 Wyrтки, K.: Indonesian through flow and the associated pressure gradient, *J. Geophys. Res.: Oceans*, 92,
798 12941-12946, <https://doi.org/10.1029/JC092iC12p12941>, 1987.
799 Xie, M., Moore, J. C., Zhao, L., Wolovick, M., and Muri, H.: Impacts of three types of solar
800 geoengineering on the Atlantic Meridional Overturning Circulation, *Atmos. Chem. Phys.*, 22,
801 4581-4597, <https://doi.org/10.5194/acp-22-4581-2022>, 2022.
802
803
804